

1

2 Modular strategies for spatial mapping of 3 multi-modal mouse brain data

4 Nicholas J. Tustison¹, Min Chen², Fae N. Kronman³, Jeffrey T. Duda², Clare Gamlin⁴, Mia
5 G. Tustison, Michael Kunst⁴, Rachel Dalley⁴, Staci Sorenson⁴, Quanxin Wang⁴, Lydia Ng⁴,
6 Yongsoo Kim³, and James C. Gee²

7 ¹Department of Radiology and Medical Imaging, University of Virginia, Charlottesville, VA

8 ²Department of Radiology, University of Pennsylvania, Philadelphia, PA

9 ³Department of Neuroscience and Experimental Therapeutics, Penn State University, Hershey, PA

10 ⁴Allen Institute for Brain Science, Seattle, WA

11

12 Corresponding authors:

13

14 Nicholas J. Tustison, DSc

15 Department of Radiology and Medical Imaging

16 University of Virginia

17 ntustison@virginia.edu

18

19 James C. Gee, PhD

20 Department of Radiology

21 University of Pennsylvania

22 gee@upenn.edu

²³ **Abstract**

²⁴ Large-scale efforts by the BRAIN Initiative Cell Census Network (BICCN) are generating a
²⁵ comprehensive reference atlas of cell types in the mouse brain. A key challenge in this effort
²⁶ is mapping diverse datasets, acquired with varied imaging, tissue processing, and profiling
²⁷ methods, into shared coordinate frameworks. Here, we present modular mapping pipelines
²⁸ developed using the Advanced Normalization Tools Ecosystem (ANTsX) to align MERFISH
²⁹ spatial transcriptomics and high-resolution fMOST morphology data to the Allen Common
³⁰ Coordinate Framework (CCFv3), and developmental MRI and LSFM data to the Devel-
³¹ opmental CCF (DevCCF). Simultaneously, we introduce two novel methods: 1) a velocity
³² field-based approach for continuous interpolation across developmental timepoints, and 2)
³³ a deep learning framework for automated brain parcellation using minimally annotated and
³⁴ publicly available data. All workflows are open-source and reproducible. We also provide
³⁵ general guidance for selecting appropriate strategies across modalities, enabling researchers
³⁶ to adapt these tools to new data.

³⁷ 1 Introduction

³⁸ Over the past decade, there have been significant advancements in mesoscopic single-cell
³⁹ analysis of the mouse brain. It is now possible to track single neurons¹, observe whole-
⁴⁰ brain developmental changes at cellular resolution², associate brain regions with genetic
⁴¹ composition³, and locally characterize neural connectivity⁴. These scientific achievements
⁴² have been propelled by high-resolution profiling and imaging techniques that enable sub-
⁴³ micron, multimodal, 3D characterizations of whole mouse brains. Among these are micro-
⁴⁴ optical sectioning tomography^{5,6}, tissue clearing methods^{1,7}, spatial transcriptomics^{8,9}, and
⁴⁵ single-cell genomic profiling¹⁰, each offering expanded specificity and resolution for cell-level
⁴⁶ brain analysis.

⁴⁷ Recent efforts by the NIH BRAIN Initiative have mobilized large-scale international collabora-
⁴⁸ tions to create a comprehensive reference database of mouse brain structure and function.
⁴⁹ The BRAIN Initiative Cell Census Network has aggregated over 40 multimodal datasets from
⁵⁰ more than 30 research groups¹¹, many of which are registered to standardized anatomical co-
⁵¹ ordinate systems to support integrated analysis. Among the most widely used of these frame-
⁵² works is the Allen Mouse Brain Common Coordinate Framework (CCFv3)¹². Other CCFs
⁵³ include modality-specific references^{13–15} and developmental atlases^{16,17} that track structural
⁵⁴ change across time.

⁵⁵ 1.1 Mouse brain mapping challenges

⁵⁶ Robust mapping of cell type data into CCFs is essential for integrative analysis of morphology,
⁵⁷ connectivity, and molecular identity. However, each modality poses unique challenges. For
⁵⁸ example, differences in tissue processing, imaging protocols, and anatomical completeness
⁵⁹ often introduce artifacts such as distortion, tearing, holes, and signal dropout^{18–23}. Inten-
⁶⁰ sity differences and partial representations of anatomy can further complicate alignment.
⁶¹ Also, while alternative strategies for mapping single-cell spatial transcriptomic data exist
⁶² (e.g., gene expression-based models such as Tangram²⁴) this work focuses on image-based
⁶³ anatomical alignment to common coordinate frameworks using spatially resolved reference

64 images. Given this diversity specialized strategies are often needed to address the unique,
65 modality-specific challenges.

66 Existing mapping solutions fall into three broad categories. The first includes integrated
67 processing platforms that provide users with mapped datasets (e.g., Allen Brain Cell
68 Atlas²⁵, Brain Architecture Portal²⁶, OpenBrainMap²⁷, and Image and Multi-Morphology
69 Pipeline²⁸). These offer convenience and high-quality curated data, but limited gener-
70 alizability and customization. The second category involves highly specialized pipelines
71 tailored to specific modalities such as histology^{29–31}, magnetic resonance imaging (MRI)^{32–34},
72 microCT^{35,36}, light sheet fluorescence microscopy (LSFM)^{37,38}, flourescence micro-optical
73 sectioning tomography (fMOST)^{15,39}, and spatial transcriptomics, including multiplexed
74 error-robust fluorescence *in situ* hybridization (MERFISH)^{40–42}. While effective, these
75 solutions often require extensive engineering effort to adapt to new datasets or modal-
76 ities. Finally, general-purpose toolkits such as elastix⁴³, Slicer3D⁴⁴, and the Advanced
77 Normalization Tools Ecosystem (ANTsX)⁴⁵ have all been applied to mouse brain mapping
78 scenarios. These toolkits support modular workflows that can be flexibly composed from
79 reusable components, offering a powerful alternative to rigid, modality-specific solutions.
80 However, their use often requires familiarity with pipeline modules, parameter tuning, and
81 tool-specific conventions which can limit adoption.

82 Building on this third category, we describe a set of modular, ANTsX-based pipelines specif-
83 ically tailored for mapping diverse mouse brain data into standardized anatomical frame-
84 works. These include two new pipelines: a velocity field-based interpolation model that
85 enables continuous transformations across developmental timepoints of the DevCCF, and a
86 template-based deep learning pipeline for whole brain segmentation (i.e., brain extraction)
87 and structural anatomical regional labeling of the brain (i.e., brain parcellation) requiring
88 minimal annotated data. In addition, we include two modular pipelines for aligning MER-
89 FISH and fMOST datasets to the Allen CCFv3. While the MERFISH dataset was previously
90 published as part of earlier BICCN efforts⁴⁶, the full image processing and registration work-
91 flow had not been described in detail until now. The fMOST workflow, by contrast, was
92 developed internally to support high-resolution morphology mapping and has not been pre-

93 viously published in any form. Both pipelines were built using ANTsX tools, adapted for
94 collaborative use with the Allen Institute, and are now released as fully reproducible, open-
95 source workflows to support reuse and extension by the community. To facilitate broader
96 adoption, we also provide general guidance for customizing these strategies across imaging
97 modalities and data types. We first introduce key components of the ANTsX toolkit, which
98 provide a basis for all of the mapping workflows described here, and then detail the specific
99 contributions made in each pipeline.

100 1.2 The Advanced Normalization Tools Ecosystem (ANTsX)

101 The Advanced Normalization Tools Ecosystem (ANTsX) has been used in a number of
102 applications for mapping mouse brain data as part of core processing steps in various
103 workflows^{31,46–49}, particularly its pairwise, intensity-based image registration capabilities⁵⁰
104 and bias field correction⁵¹. Historically, ANTsX development is based on foundational ap-
105 proaches to image mapping^{52–54}, especially in the human brain, with key contributions such
106 as the Symmetric Normalization (SyN) algorithm⁵⁰. It has been independently evaluated
107 in diverse imaging domains including multi-site brain MRI⁵⁵, pulmonary CT⁵⁶, and multi-
108 modal brain tumor registration⁵⁷. More recent contributions for mouse-specific applications
109 showcase multimodal template generation¹⁶ and anatomy-aware registration⁵⁸ ANTsX func-
110 tionality.

111 Beyond registration, ANTsX provides functionality for template generation⁵⁹, segmentation⁶⁰,
112 preprocessing^{51,61}, and deep learning⁴⁵. It has demonstrated strong performance in consen-
113 sus labeling⁶², brain tumor segmentation⁶³, and cardiac motion estimation⁶⁴. Built on the
114 Insight Toolkit (ITK)⁶⁵, ANTsX benefits from open-source contributions while supporting
115 continued algorithm evaluation and innovation. In the context of mouse brain data, ANTsX
116 provides a robust platform for developing modular pipelines to map diverse imaging modal-
117 ities into CCFs. These tools span multiple classes of mapping problems: cross-modality
118 image registration, landmark-driven alignment, temporal interpolation across developmental
119 stages, and deep learning-based segmentation. As such, they also serve as illustrative case
120 studies for adapting ANTsX tools to other use cases. We describe both shared infrastructure

121 and targeted strategies adapted to the specific challenges of each modality. This paper
122 highlights usage across distinct BICCN projects such as spatial transcriptomic data from
123 MERFISH, structural data from fMOST, and multimodal developmental data from LSFM
124 and MRI.

125 **1.3 Novel ANTsX-based open-source contributions**

126 We introduce two novel contributions to ANTsX developed as part of collaborative efforts
127 in creating the Developmental Common Coordinate Framework (DevCCF)¹⁶. First, we
128 present an open-source velocity field-based interpolation framework for continuous map-
129 ping across the sampled embryonic and postnatal stages of the DevCCF atlas¹⁶. This
130 functionality enables biologically plausible interpolation between timepoints via a time-
131 parameterized diffeomorphic velocity model⁶⁶, inspired by previous work⁶⁷. Second, we
132 present a deep learning pipeline for structural parcellation of the mouse brain from mul-
133 timodal MRI data. This includes two novel components: 1) a template-derived brain ex-
134 traction model using augmented data from two ANTsX-derived template datasets^{68,69}, and
135 2) a template-derived parcellation model trained on DevCCF P56 labelings mapped from
136 the AllenCCFv3. This pipeline demonstrates how ANTsX tools and public resources can be
137 leveraged to build robust anatomical segmentation pipelines with minimal annotated data.
138 We independently evaluate this framework using a longitudinal external dataset⁷⁰, demon-
139 strating generalizability across specimens and imaging protocols. All components are openly
140 available through the R and Python ANTsX packages, with general-purpose functionality
141 documented in a reproducible, cross-platform tutorial (<https://tinyurl.com/antsxtutorial>).
142 Code specific to this manuscript, including scripts to reproduce the novel contributions
143 and all associated evaluations, is provided in a dedicated repository (<https://github.com/>
144 [ntustison/ANTsXMouseBrainMapping](https://github.com/ntustison/ANTsXMouseBrainMapping)). Additional tools for mapping spatial transcriptomic
145 (MERFISH) and structural (fMOST) data to the AllenCCFv3 are separately available at
146 (<https://github.com/dontminchenit/CCFAlignmentToolkit>).

2 Results

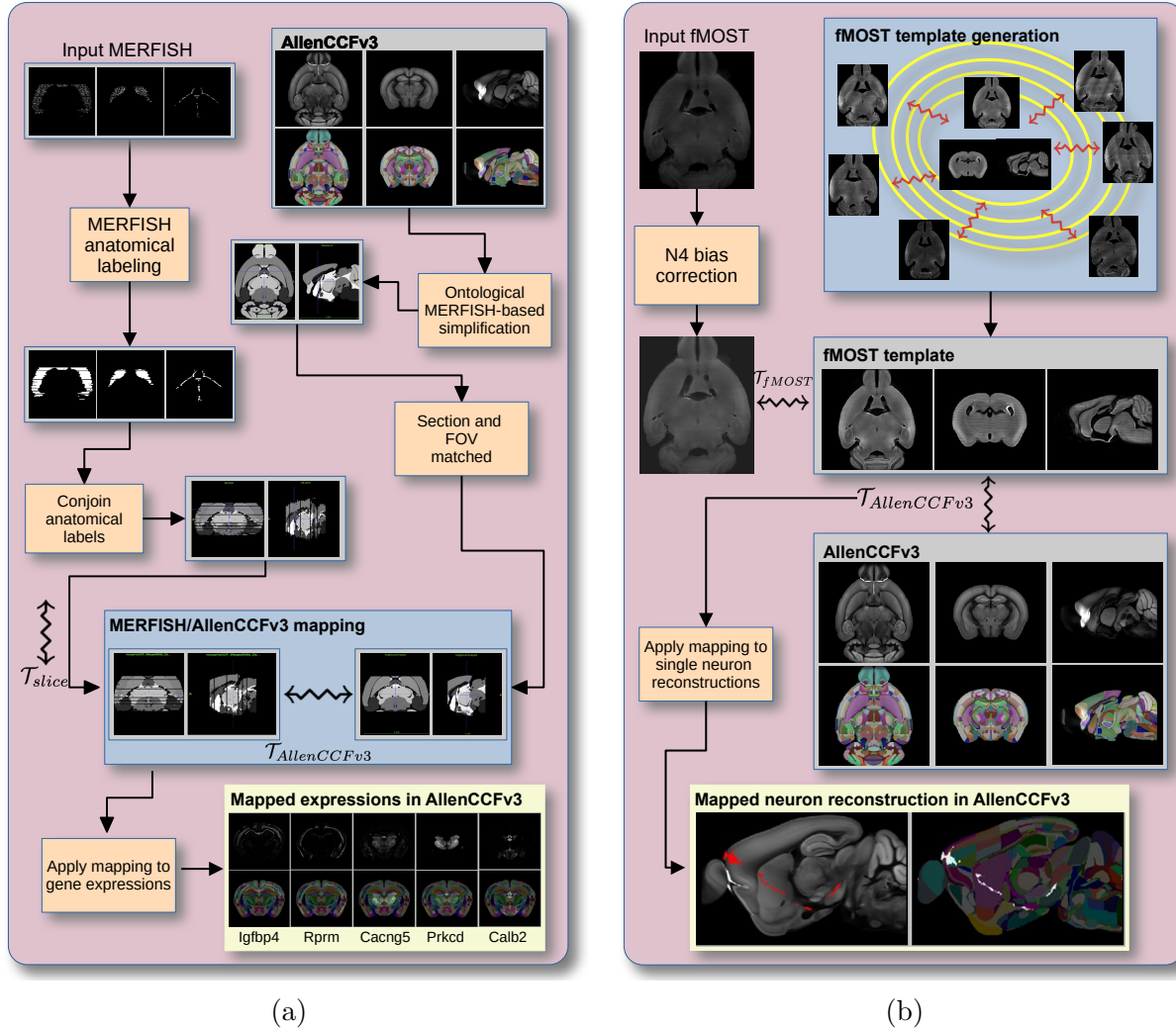


Figure 1: Diagram of the two ANTsX-based pipelines for mapping (a) MERFISH and (b)fMOST data into the space of AllenCCFv3. Each generates the requisite transforms to map individual images to the CCF.

2.1 AllenCCFv3 brain image mapping

2.1.1 Mapping multiplexed error-robust fluorescence *in situ* hybridization (MERFISH) data

Overview. We developed an ANTsX-based pipeline to map spatial transcriptomic MERFISH data into the AllenCCFv3 (Figure 1(a)). This approach was used in recent efforts to

153 create a high-resolution transcriptomic atlas of the mouse brain⁴⁶. The pipeline maps spa-
154 tial gene expression patterns from MERFISH onto anatomical labels in the AllenCCFv3. It
155 includes MERFISH-specific preprocessing steps such as section reconstruction, label genera-
156 tion from spatial transcriptomic maps, and anatomical correspondence mapping. Alignment
157 proceeds in two stages: 1) 3D affine registration and section matching of the AllenCCFv3 to
158 the MERFISH data, and 2) linear + deformable 2D section-wise alignment between matched
159 MERFISH and atlas slices. These transformations are concatenated to produce a complete
160 mapping from each MERFISH data to AllenCCFv3.

161 **Data.** MERFISH imaging was performed on cryosectioned brains from C57BL/6 mice using
162 previously described protocols⁴⁶. Brains were placed into an optimal cutting temperature
163 (OCT) compound (Sakura FineTek 4583) stored at -80°. The fresh frozen brain was sectioned
164 at 10 μm on Leica 3050 S cryostats at intervals of 200 μm to evenly cover the brain. A set
165 of 500 genes was selected to distinguish \sim 5200 transcriptomic clusters. Raw MERSCOPE
166 data were decoded using Vizgen software (v231). Cell segmentation was performed using
167 Cellpose^{71,72} based on DAPI and PolyT stains which was propagated to adjacent slices across
168 z-planes. Each MERFISH cell was assigned a transcriptomic identity by mapping to a
169 scRNA-seq reference taxonomy.

170 **Evaluation.** Alignment quality was evaluated iteratively by an expert anatomist, guided
171 by expected gene-marker correspondences to AllenCCFv3 regions. As previously reported⁴⁶,
172 further assessment of the alignment showed that, of the 554 terminal regions (gray matter
173 only in the AllenCCFv3), only seven small subregions did not contain cells from the MER-
174 FISH dataset post registration: frontal pole, layer 1 (FRP1), FRP2/3, FRP5; accessory
175 olfactory bulb, glomerular layer (AOBgl); accessory olfactory bulb, granular layer (AOBgr);
176 accessory olfactory bulb, mitral layer (AOBmi); and accessory supraoptic group (ASO). A
177 broader discussion of evaluation design choices and evaluation rationale is included in the
178 Discussion.

¹⁷⁹ **2.1.2 Mapping fluorescence micro-optical sectioning tomography (fMOST) data**

¹⁸⁰ **Overview.** We also constructed a pipeline for mapping fMOST images to the AllenCCFv3
¹⁸¹ using ANTsX (Figure 1(b)). The approach leverages a modality-specific average fMOST
¹⁸² atlas as an intermediate target, adapted from previous work in human and mouse brain
¹⁸³ mapping^{12,15,16,59,73–76}. The atlas was constructed from 30 fMOST images selected to cap-
¹⁸⁴ ture representative variability in anatomical shape and image intensity across the population.
¹⁸⁵ Preprocessing includes cubic B-spline downsampling to match the 25 μm isotropic AllenC-
¹⁸⁶ CCFv3 resolution, stripe artifact suppression using a 3D notch filter implemented with SciPy’s
¹⁸⁷ frequency-domain filtering tools, and N4 bias field correction⁵¹. A one-time, annotation-
¹⁸⁸ driven alignment registers the fMOST atlas to AllenCCFv3 using landmark-based registra-
¹⁸⁹ tion of key structures. This canonical mapping is then reused. New fMOST specimens are
¹⁹⁰ first aligned to the fMOST atlas using standard intensity-based registration, and the con-
¹⁹¹ catenated transforms yield full spatial normalization to the AllenCCFv3. This same mapping
¹⁹² can be applied to neuron reconstructions to facilitate population-level analysis of morphology
¹⁹³ and spatial distribution.

¹⁹⁴ **Data.** fMOST imaging was performed on 55 mouse brains with sparse transgenic labeling
¹⁹⁵ of neuron populations^{77,78} using the high-throughput fMOST platform^{79,80}. Voxel resolution
¹⁹⁶ was $0.35 \times 0.35 \times 1.0 \mu\text{m}^3$. Two imaging channels were acquired: GFP-labeled neuron mor-
¹⁹⁷ phology (green), and propidium iodide counterstaining for cytoarchitecture (red). Alignment
¹⁹⁸ was performed using the red channel for its greater contrast, though multi-channel mapping
¹⁹⁹ is also supported.

²⁰⁰ **Evaluation.** The canonical mapping from the fMOST atlas to AllenCCFv3 was eval-
²⁰¹ uated using both quantitative and qualitative approaches. Dice similarity coefficients were
²⁰² computed between corresponding anatomical labels in the fMOST atlas and AllenCCFv3
²⁰³ following registration. These labels were manually annotated or adapted from existing atlas
²⁰⁴ segmentations. Representative Dice scores included: whole brain (0.99), caudate putamen
²⁰⁵ (0.97), fimbria (0.91), posterior choroid plexus (0.93), anterior choroid plexus (0.96), optic
²⁰⁶ chiasm (0.77), and habenular commissure (0.63). In addition to these quantitative assess-
²⁰⁷ ments, each registered fMOST specimen was evaluated qualitatively. An expert anatomist

208 reviewed alignment accuracy and confirmed structural correspondence. Neuron reconstruc-
209 tions from individual brains were also transformed into AllenCCFv3 space, and their traject-
210 ories were visually inspected to confirm anatomical plausibility and preservation of known
211 projection patterns. A broader discussion of evaluation design choices and evaluation ratio-
212 nale is included in the Discussion.

213 **2.2 Continuously mapping the DevCCF developmental trajectory**

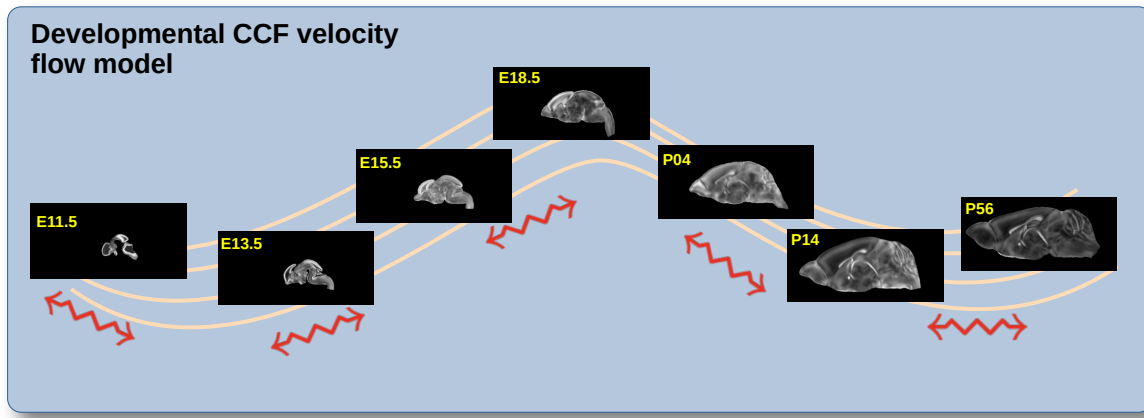


Figure 2: The spatial transformation between any two time points within the continuous DevCCF longitudinal developmental trajectory is available through the use of ANTsX functionality for generating a velocity flow model.

214 The DevCCF is an openly accessible resource for the mouse brain research community¹⁶,
215 comprising symmetric, multi-modal MRI and LSFM templates generated using the ANTsX
216 framework⁵⁹. It spans key stages of mouse brain development (E11.5, E13.5, E15.5, E18.5,
217 P4, P14, and P56) and includes structural labels defined by a developmental ontology.
218 The DevCCF was constructed in coordination with the AllenCCFv3 to facilitate integra-
219 tion across atlases and data types.

220 Although this collection provides broad developmental coverage, its discrete sampling
221 limits the ability to model continuous transformations across time. To address this, we
222 developed a velocity flow-based modeling approach that enables anatomically plausible,
223 diffeomorphic transformations between any two continuous time points within the De-

vCCF range. Unlike traditional pairwise interpolation, which requires sequential warping through each intermediate stage, this model, defined by a time-varying velocity field (i.e., a smooth vector field defined over space and time that governs the continuous deformation of an image domain), allows direct computation of deformations between any two time points in the continuum which improves smoothness and enables flexible spatiotemporal alignment. This functionality is implemented in both ANTsR and ANTsPy (see `ants.fit_time_varying_transform_to_point_sets(...)`) and integrates seamlessly with existing ANTsX workflows. The velocity field is represented as a 4D ITK image where each voxel stores the x,y,z components of motion at a given time point. Integration of the time-varying velocity field uses uses 4th order Runge-Kutta (`ants.integrate_velocity_field(...)`)⁸¹.

2.2.1 Data

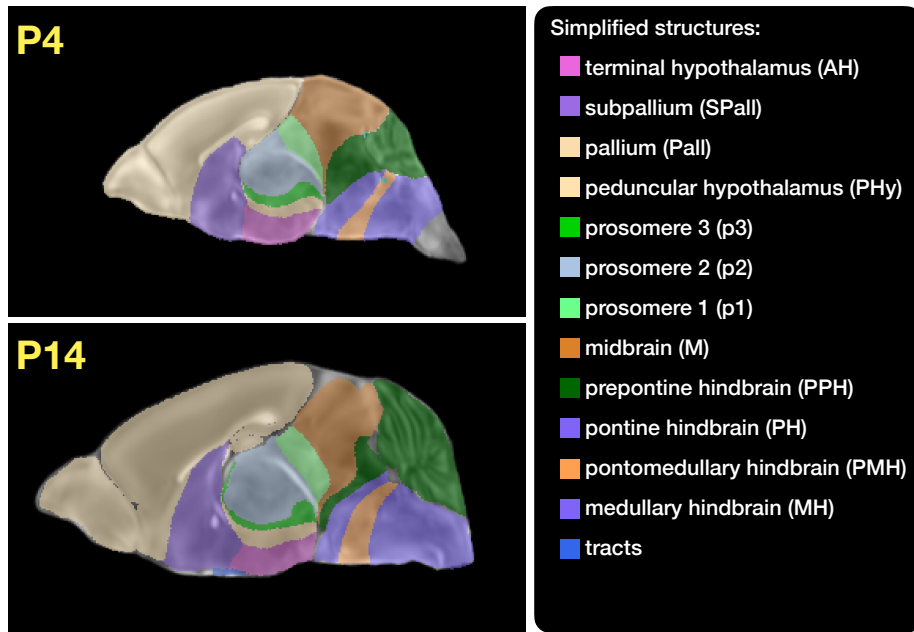


Figure 3: Annotated regions representing common labels across developmental stages, shown for both P4 and P14.

Each DevCCF template includes over 2,500 labeled anatomical regions, with spatial resolutions ranging from 31.5 to 50 μ m. For the velocity flow modeling task, we identified a common set of 26 bilateral regions (13 per hemisphere) that were consistently labeled across

239 all timepoints. These regions span major developmental domains including the pallium, sub-
240 pallium, midbrain, prosomeres, hypothalamus, hindbrain subregions, and key white matter
241 tracts (Figure 3).

242 Prior to velocity field optimization, all templates were rigidly aligned to the DevCCF P56
243 template using the centroids of these common label sets. Pairwise correspondence be-
244 tween adjacent timepoints was then computed using ANTsX’s multi-metric registration via
245 `ants.registration(...)`. Instead of performing intensity-based multi-label registration di-
246 rectly, we constructed 24 binary label masks per atlas pair (one per structure) and optimized
247 alignment using the mean squares similarity metric with the SyN transform⁵⁰.

248 To generate the point sets for velocity field optimization, we sampled both boundary (con-
249 tour) and interior (region) points from the P56 labels and propagated them to each devel-
250 opmental stage using the learned pairwise transforms. Contours were sampled at 10% of
251 available points and regions at 1%, yielding 173,303 total points per atlas ($N_{contour} = 98,151$;
252 $N_{region} = 75,152$). Boundary points were assigned double weight during optimization to
253 emphasize anatomical boundary correspondence.

254 2.2.2 Velocity field optimization

255 The velocity field was optimized using the seven corresponding point sets and their associated
256 weights. The field geometry was defined at [256, 182, 360] with 11 integration points at 50
257 μm resolution, yielding a compressed velocity model of ~ 2 GB. This resolution balanced
258 accuracy and computational tractability while remaining portable. All data and code are
259 publicly available in the accompanying GitHub repository.

260 To normalize temporal spacing, we assigned scalar values in [0, 1] to each template. Given
261 the nonlinear spacing in postnatal development, we applied a logarithmic transform to the
262 raw time values prior to normalization. Within this logarithmic temporal transform, P56
263 was assigned a span of 28 postnatal days to reflect known developmental dynamics (i.e., in
264 terms of modeling the continuous deformation, the morphological changes between Day 28
265 and Day 56 are insignificant). This improved the temporal distribution of integration points
266 (Figure 4, right panel).

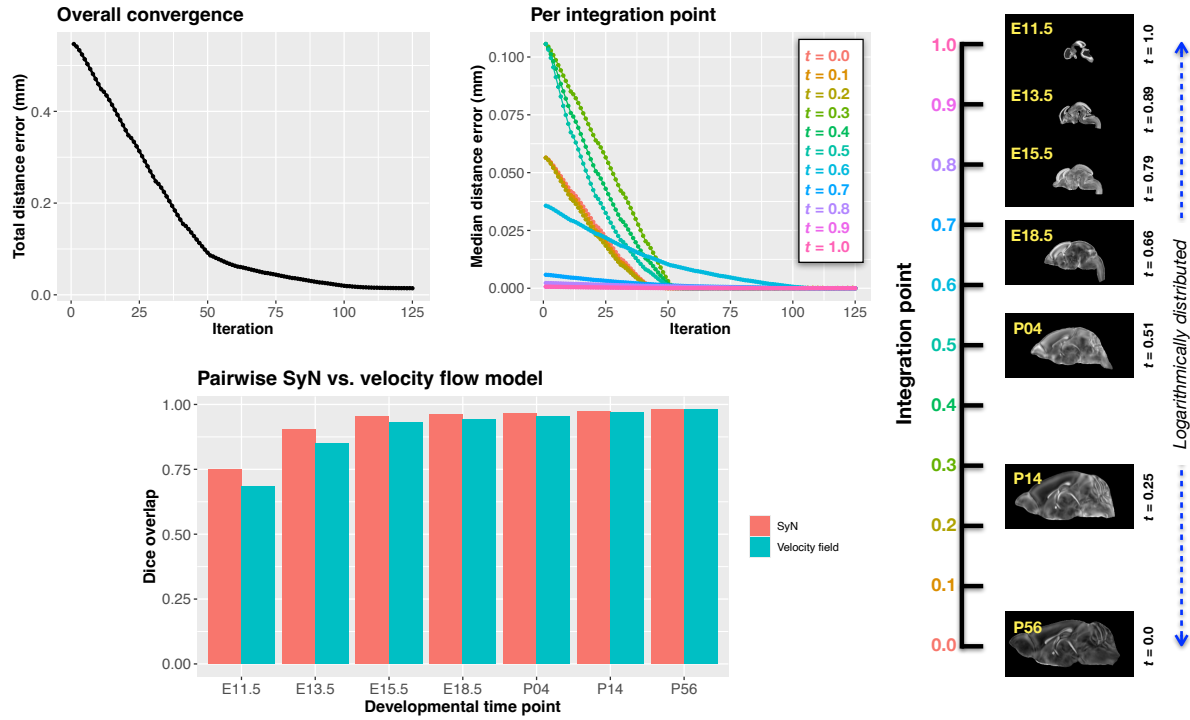


Figure 4: Convergence and evaluation of the velocity flow model across the DevCCF developmental trajectory. (Top left) Total displacement error over iterations. (Top right) Median displacement error per integration point across the optimization timeline, spanning embryonic (E11.5) to postnatal (P56) stages. (Bottom) Dice similarity scores comparing region-level label overlap between: (1) conventional pairwise SyN registration and (2) velocity flow-based deformation, across intermediate timepoints. Using region-based pairwise registration with SyN as a performance upper bound, the velocity flow model achieves comparable accuracy while also enabling smooth, continuous deformation across the full developmental continuum.

Optimization was run for a maximum of 200 iterations using a 2020 iMac (3.6 GHz 10-Core Intel Core i9, 64 GB RAM), with each iteration taking ~ 6 minutes. During each iteration, the velocity field was updated across all 11 integration points by computing regularized displacement fields between warped point sets at adjacent time slices. Updates were applied using a step size of $\delta = 0.2$. Convergence was assessed via average displacement error across all points, with final convergence achieved after ~ 125 iterations (Figure 4, left panel). Median errors across integration points also trended toward zero, albeit at varying rates. To benchmark performance, we compared the velocity model's region-based alignment to traditional pairwise registration using SyN, a widely used diffeomorphic algorithm. The velocity model achieved comparable Dice scores at sampled timepoints while additionally

277 offering smooth interpolation across the entire developmental trajectory.

278 **2.2.3 The velocity flow transformation model**

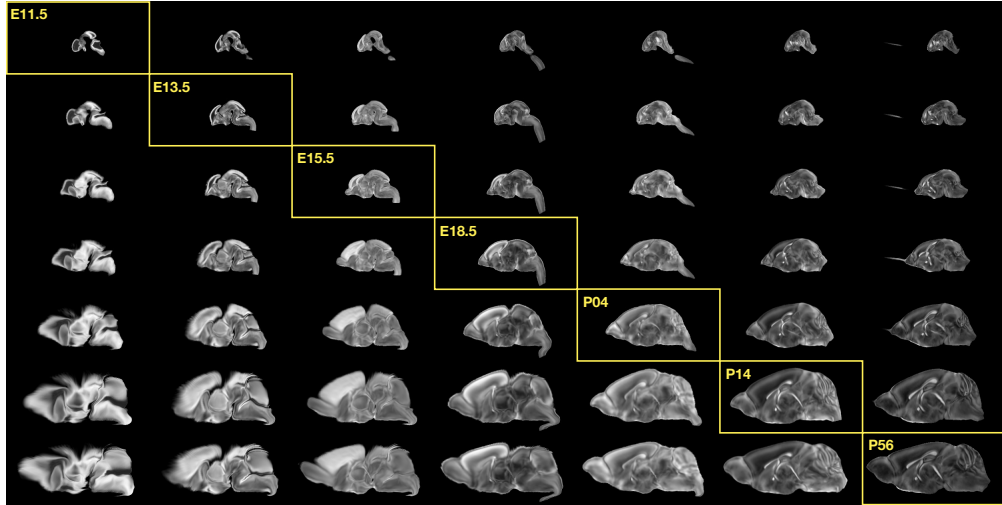


Figure 5: Mid-sagittal visualization of DevCCF templates warped to every other time point. Each row is a reference space; each column is a warped input. Diagonal entries show original templates.

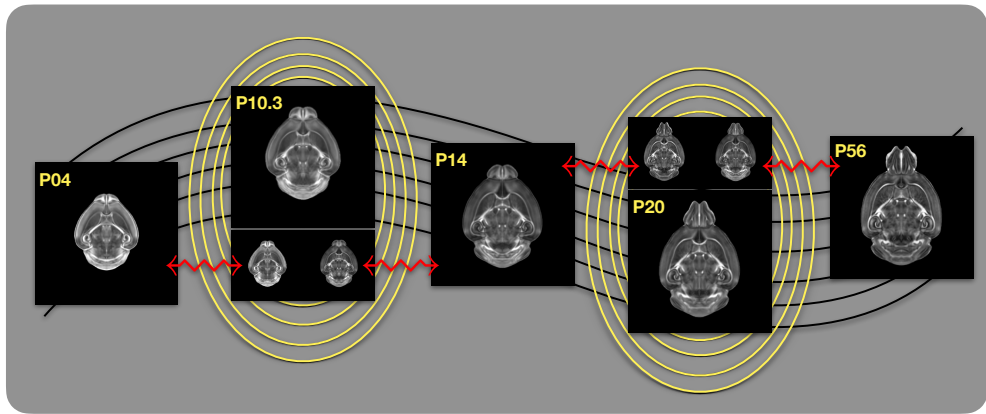


Figure 6: Example of generating “virtual” DevCCF templates at intermediate time points (e.g., P10.3, P20) by warping adjacent stages to a shared time and averaging using ANTsX.

279 Once optimized, the velocity field enables the computation of diffeomorphic transformations
280 between any pair of continuous time points within the DevCCF developmental range. Fig-
281 ure 5 illustrates cross-warping between all DevCCF stages using the velocity flow model. In
282 addition to facilitating flexible alignment between existing templates, the model also sup-

283 ports the synthesis of virtual templates at intermediate, unsampled developmental stages.
 284 As shown in Figure 6, we demonstrate the creation of virtual age templates (e.g., P10.3 and
 285 P20) by warping adjacent developmental atlases to a target timepoint and constructing an
 286 averaged representation using ANTsX’s template-building functionality.
 287 All usage examples, scripts, and supporting data for full reproducibility are publicly available
 288 in the associated codebase.

289 2.3 Automated structural labeling of the mouse brain

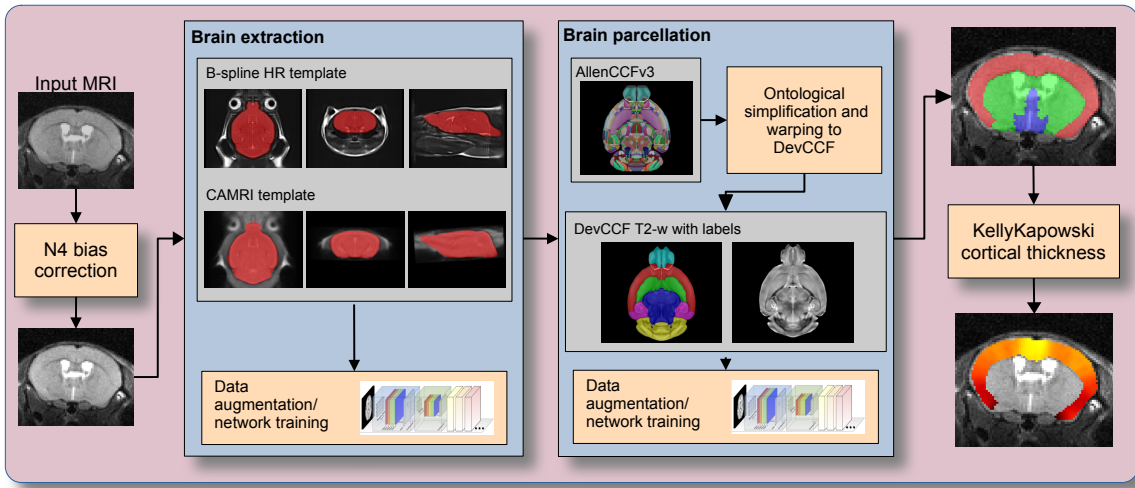


Figure 7: The mouse brain cortical labeling pipeline integrates two deep learning components for brain extraction and anatomical region segmentation. Both networks rely heavily on data augmentation applied to templates constructed from open datasets. The framework also supports further refinement or alternative label sets tailored to specific research needs. Possible applications include voxelwise cortical thickness estimation.

290 Structural labeling strategies for the mouse brain are essential for understanding the organiza-
 291 tion and function of the murine nervous system⁸². By dividing the brain into anatomically
 292 or functionally defined regions, researchers can localize biological processes, relate regional
 293 features to behavior, or quantify spatial variation in gene expression patterns^{83,84}. While
 294 deep learning techniques have yielded robust segmentation and labeling tools for the hu-
 295 man brain (e.g., SynthSeg⁸⁵, ANTsXNet⁴⁵), analogous development for mouse data (e.g.,
 296 MEMOS⁸⁶) has been limited. Mouse neuroimaging often presents unique challenges, such

as highly anisotropic sampling, that complicate transfer of existing tools. At the same time, high resolution resources like the AllenCCFv3 and DevCCF provide reference label sets that can serve as training data. We demonstrate how ANTsX can be used to construct a full structural labeling pipeline for the mouse brain (Figure 7), including both whole brain segmentation (i.e., brain extraction) and the subsequent template-based region segmentation.

2.3.1 Template-based mouse brain extraction network

To develop a general-purpose mouse brain extraction model, we constructed whole-head templates from two publicly available T2-weighted datasets. The first dataset, from the Center for Animal MRI (CAMRI) at the University of North Carolina at Chapel Hill⁶⁸, includes 16 isotropic MRI volumes acquired at $0.16 \times 0.16 \times 0.16$ mm³ resolution. The second dataset⁶⁹ comprises 88 specimens acquired in three orthogonal 2D views (coronal, axial, sagittal) at 0.08×0.08 mm³ in-plane resolution with 0.5 mm slice thickness. These orthogonal 2D acquisitions were reconstructed into high-resolution 3D volumes using a B-spline fitting algorithm⁸⁷. Using this synthesized dataset and the CAMRI images, we created two ANTsX-based population templates⁵⁹, each paired with a manually delineated brain mask. These served as the basis for training an initial template-based brain extraction model. Deep learning training of the network employed aggressive data augmentation strategies, including bias field simulation, histogram warping, random spatial deformation, noise injection, and anisotropic resampling. This enabled the model to generalize beyond the two templates. The initial model was released through ANTsXNet and made publicly available.

Subsequent community use led to further improvements. A research group applying the tool to their own ex vivo T2-weighted mouse brain data contributed a third template and associated mask (acquired at 0.08 mm isotropic resolution). Incorporating this into the training data improved robustness and accuracy to an independent dataset and extended the model’s generalizability. The refined model is distributed through ANTsPyNet via `antspynet.mouse_brain_extraction(...)`.

323 **2.3.2 Template-based mouse brain anatomical labeling**

324 The AllenCCFv3 atlas and its hierarchical ontology, along with the DevCCF, provide a strong
325 foundation for developing region-wise anatomical labeling models for multi-modal mouse
326 brain imaging. Using the `allensdk` Python library, we generated a coarse segmentation
327 scheme by grouping anatomical labels into six major regions: cerebral cortex, cerebral nuclei,
328 brainstem, cerebellum, main olfactory bulb, and hippocampal formation. These labels were
329 mapped onto the P56 T2-weighted DevCCF template to serve as training targets. We trained
330 a 3D U-net-based segmentation network using this template and the same augmentation
331 strategies described for brain extraction. The model is publicly available via ANTsXNet
332 (`antspynet.mouse_brain_parcellation(...)`) and supports robust anatomical labeling
333 across diverse imaging geometries and contrasts. The inclusion of aggressive augmentation,
334 including simulated anisotropy, enables the model to perform well even on thick-slice input
335 data. Internally, the model reconstructs isotropic probability and label maps, facilitating
336 downstream morphometric analyses. For example, this network integrates with the ANTsX
337 cortical thickness estimation pipeline (`antspynet.mouse_cortical_thickness(...)`) to
338 produce voxelwise cortical thickness maps, even when applied to anisotropic or limited-
339 resolution mouse brain data.

340 **2.3.3 Evaluation**

341 For evaluation, we used an additional publicly available dataset⁷⁰ that is completely inde-
342 pendent from the data used in training the brain extraction and parcellation networks. Data
343 includes 12 specimens each imaged at seven time points (Day 0, Day 3, Week 1, Week 4,
344 Week 8, Week 20) with in-house-generated brain masks (i.e., produced by the data providers)
345 for a total of 84 images. Spacing is anistropic with an in-plane resolution of $0.1 \times 0.1 \text{ mm}^2$
346 and a slice thickness of 0.5 mm.

347 Figure 8 summarizes the whole-brain overlap between manually segmented reference masks
348 and the predicted segmentations for all 84 images in the evaluation cohort. The proposed
349 network demonstrates excellent performance in brain extraction across a wide age range. To

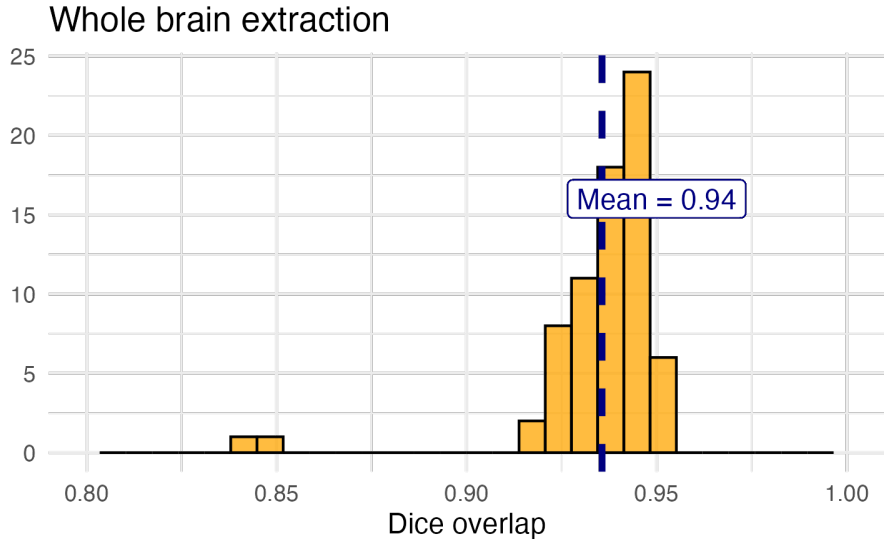
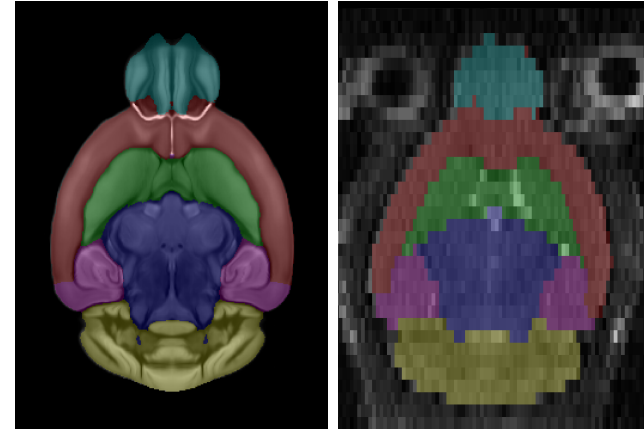


Figure 8: Evaluation of the ANTsX mouse brain extraction on an independent, publicly available dataset consisting of 12 specimens \times 7 time points = 84 total images. Dice overlap comparisons with the user-generated brain masks provide good agreement with the automated results from the brain extraction network.

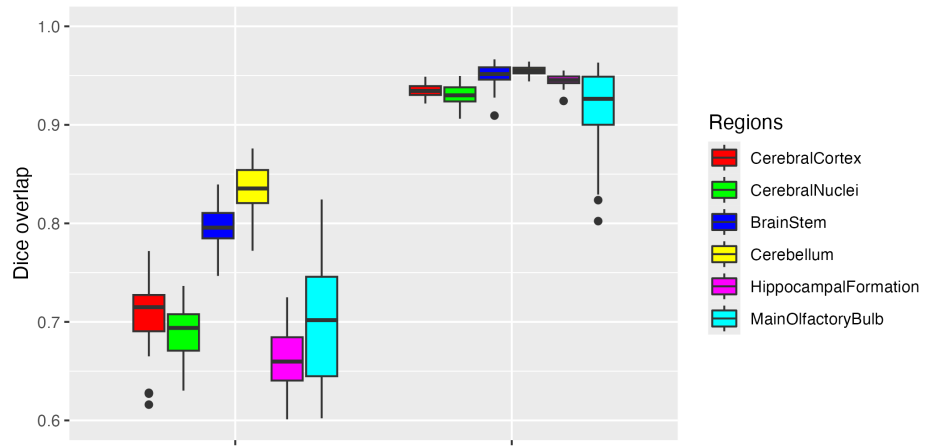
350 further assess the utility of the parcellation network, we used the predicted labels to guide
 351 anatomically informed registration to the AllenCCFv3 atlas using ANTsX multi-component
 352 registration, and compared this to intensity-only registration (Figure 9). While intensity-
 353 based alignment performs reasonably well, incorporating the predicted parcellation signifi-
 354 cantly improves regional correspondence. Dice scores shown in Figure 9(c) were computed
 355 using manually segmented labels transformed to AllenCCFv3 space.



(a)

(b)

Normalization to AllenCCFv3



(c)

Figure 9: Evaluation of the ANTsX deep learning-based mouse brain parcellation on a diverse MRI cohort. (a) T2-weighted DevCCF P56 template with the six-region parcellation: cerebral cortex, nuclei, brain stem, cerebellum, main olfactory bulb, and hippocampal formation. (b) Example segmentation result from a representative subject (NR5, Day 0) using the proposed deep learning pipeline. (c) Dice overlap scores across the full evaluation cohort ($n = 84$), comparing anatomical alignment achieved via registration using intensity alone versus registration guided by the predicted parcellation. Dice values were computed using manually segmented labels transformed to AllenCCFv3 space.

³⁵⁶ **3 Discussion**

³⁵⁷ The diverse mouse brain cell type profiles gathered through BICCN and associated efforts
³⁵⁸ provide a rich multi-modal resource to the research community. However, despite significant
³⁵⁹ progress, optimal leveraging of these valuable resources remains an ongoing challenge. A
³⁶⁰ central component to data integration is accurately mapping novel cell type data into com-
³⁶¹ mon coordinate frameworks (CCFs) for subsequent processing and analysis. To meet these
³⁶² needs, tools for mapping mouse brain data must be both broadly accessible and capable of
³⁶³ addressing challenges unique to each modality. In this work, we described modular ANTsX-
³⁶⁴ based pipelines developed to support three distinct BICCN efforts encompassing spatial
³⁶⁵ transcriptomic, morphological, and developmental data. We demonstrated how a flexible
³⁶⁶ image analysis toolkit like ANTsX can be tailored to address specific modality-driven con-
³⁶⁷ straints by leveraging reusable, validated components.

³⁶⁸ As part of collaborative efforts with the Allen Institute for Brain Science and the broader
³⁶⁹ BICCN initiative, we developed two modular pipelines for mapping MERFISH and fMOST
³⁷⁰ datasets to the AllenCCFv3. These workflows were designed to accommodate the spe-
³⁷¹ cific requirements of high-resolution transcriptomic and morphological data while leveraging
³⁷² reusable components from the ANTsX ecosystem. The MERFISH pipeline incorporates
³⁷³ preprocessing and registration steps tailored to known anatomical and imaging artifacts in
³⁷⁴ multiplexed spatial transcriptomic data. While the general mapping strategy is applicable
³⁷⁵ to other sectioned histological datasets, these refinements demonstrate how general-purpose
³⁷⁶ tools can be customized to meet the demands of specialized modalities. The fMOST work-
³⁷⁷ flow, in contrast, emphasizes reusability and consistency across large datasets. It introduces
³⁷⁸ an intermediate, canonical fMOST atlas to stabilize transformations to the AllenCCFv3,
³⁷⁹ reducing the need for repeated manual alignment and enabling standardized mapping of
³⁸⁰ single-neuron reconstructions to a common coordinate framework.

³⁸¹ Evaluation of both workflows followed established QA/QC protocols used at the Allen In-
³⁸² stitute, emphasizing biologically meaningful criteria such as expected gene-marker align-
³⁸³ ment (MERFISH) and accurate reconstruction of neuronal morphology (fMOST). These
³⁸⁴ domain-informed assessments, also used in prior large-scale mapping projects⁴⁶, prioritize

385 task-relevant accuracy over other possible benchmarks such as Dice coefficients or landmark
386 distances. While formal quantitative scores were not reported for these specific pipelines,
387 they both demonstrate reliable, expert-validated performance in collaborative contexts. Ad-
388 ditional documentation and evaluation commentary are available in the updated CCFAlign-
389 mentToolkit GitHub repository.

390 For developmental data, we introduced a velocity field-based model for continuous interpo-
391 lation between discrete DevCCF timepoints. Although the DevCCF substantially expands
392 coverage of developmental stages relative to prior atlases, temporal gaps remain. The ve-
393 locity model enables spatio-temporal transformations within the full developmental interval
394 and supports the generation of virtual templates at unsampled ages. This functionality is
395 built using ANTsX components for velocity field optimization and integration, and offers
396 a novel mechanism for interpolating across the non-linear developmental trajectory of the
397 mouse brain. Such interpolation has potential utility for both anatomical harmonization and
398 longitudinal analyses. Interestingly, long-range transformations (e.g., P56 to E11.5) revealed
399 anatomy evolving in plausible ways yet sometimes diverging from known developmental pat-
400 terns (e.g., hippocampal shape changes) reflecting the input data and offering insight into
401 temporal gaps. These behaviors could assist future efforts to determine which additional
402 time points would most improve spatiotemporal coverage.

403 We also introduced a template-based deep learning pipeline for mouse brain extraction and
404 parcellation using aggressive data augmentation. This approach is designed to reduce the
405 reliance on large annotated training datasets, which remain limited in the mouse imaging
406 domain. Evaluation on independent data demonstrates promising generalization, though
407 further refinement will be necessary. As with our human-based ANTsX pipelines, failure
408 cases can be manually corrected and recycled into future training cycles. Community con-
409 tributions are welcomed and encouraged, providing a pathway for continuous improvement
410 and adaptation to new datasets.

411 The ANTsX ecosystem offers a powerful foundation for constructing scalable, reproducible
412 pipelines for mouse brain data analysis. Its modular design and multi-platform support
413 enable researchers to develop customized workflows without extensive new software devel-

⁴¹⁴ opment. The widespread use of ANTsX components across the neuroimaging community
⁴¹⁵ attests to its utility and reliability. As a continuation of the BICCN program, ANTsX is
⁴¹⁶ well positioned to support the goals of the BRAIN Initiative Cell Atlas Network (BICAN)
⁴¹⁷ and future efforts to extend these mapping strategies to the human brain.

418 **4 Methods**

419 The following methods are all available as part of the ANTsX ecosystem with analogous
420 elements existing in both ANTsR (ANTs in R) and ANTsPy (ANTs in Python), under-
421 pinned by a shared ANTs/ITK C++ core. Most development for the work described was
422 performed using ANTsPy. For equivalent functionality in ANTsR, we refer the reader to the
423 comprehensive ANTsX tutorial: <https://tinyurl.com/antsxtutorial>.

424 **4.1 General ANTsX utilities**

425 Although focused on distinct data types, the three pipelines presented in this work share
426 common components that address general challenges in mapping mouse brain data. These
427 include correcting image intensity artifacts, denoising, spatial registration, template gen-
428 eration, and visualization. Table 1 provides a concise summary of the relevant ANTsX
429 functionality.

430 **Preprocessing: bias field correction and denoising.** Standard preprocessing steps in
431 mouse brain imaging include correcting for spatial intensity inhomogeneities and reducing im-
432 age noise, both of which can impact registration accuracy and downstream analysis. ANTsX
433 provides implementations of widely used methods for these tasks. The N4 bias field correction
434 algorithm⁵¹, originally developed in ANTs and contributed to ITK, mitigates artifactual, low-
435 frequency intensity variation and is accessible via `ants.n4_bias_field_correction(...)`.
436 Patch-based denoising⁶¹ has been implemented as `ants.denoise_image(...)`.

437 **Image registration.** ANTsX includes a robust and flexible framework for pairwise
438 and groupwise image registration⁸¹. At its core is the SyN algorithm⁵⁰, a symmetric
439 diffeomorphic model with optional B-spline regularization⁶⁷. In ANTsPy, registration
440 is performed via `ants.registration(...)` using preconfigured parameter sets (e.g.,
441 `antsRegistrationSyNQuick[s]`, `antsRegistrationSyN[s]`) suitable for different imaging
442 modalities and levels of computational demand. Resulting transformations can be applied
443 to new images with `ants.apply_transforms(...)`.

Table 1: Sampling of ANTsX functionality

<i>ANTsPy: Preprocessing</i>	
bias field correction	<code>n4_bias_field_correction(...)</code>
image denoising	<code>denoise_image(...)</code>
<i>ANTsPy: Registration</i>	
intensity image registration	<code>registration(...)</code>
label image registration	<code>label_image_registration(...)</code>
image transformation	<code>apply_transforms(...)</code>
template generation	<code>build_template(...)</code>
landmark registration	<code>fit_transform_to_paired_points(...)</code>
time-varying landmark reg.	<code>fit_time_varying_transform_to_point_sets(...)</code>
integrate velocity field	<code>integrate_velocity_field(...)</code>
invert displacement field	<code>invert_displacement_field(...)</code>
<i>ANTsPy: Segmentation</i>	
MRF-based segmentation	<code>atropos(...)</code>
Joint label fusion	<code>joint_label_fusion(...)</code>
diffeomorphic thickness	<code>kelly_kapowski(...)</code>
<i>ANTsPy: Miscellaneous</i>	
Regional intensity statistics	<code>label_stats(...)</code>
Regional shape measures	<code>label_geometry_measures(...)</code>
B-spline approximation	<code>fit_bspline_object_to_scattered_data(...)</code>
Visualize images and overlays	<code>plot(...)</code>
<i>ANTsPyNet: Mouse-specific</i>	
brain extraction	<code>mouse_brain_extraction(...modality="t2"...)</code>
brain parcellation	<code>mouse_brain_parcellation(...)</code>
cortical thickness	<code>mouse_cortical_thickness(...)</code>
super resolution	<code>mouse_histology_super_resolution(...)</code>

ANTsX provides state-of-the-art functionality for processing biomedical image data. Such tools, including deep learning networks, support a variety of mapping-related tasks. A more comprehensive listing of ANTsX tools with self-contained R and Python examples is provided as a gist page on GitHub (<https://tinyurl.com/antsxtutorial>).

444 **Template generation.** ANTsX supports population-based template generation through it-
445 erative pairwise registration to an evolving estimate of the mean shape and intensity reference
446 space across subjects⁵⁹. This functionality was used in generating the DevCCF templates¹⁶.
447 The procedure, implemented as `ants.build_template(...)`, produces average images in
448 both shape and intensity by aligning all inputs to a common evolving template.

449 **Visualization.** To support visual inspection and quality control, ANTsPy provides flexible
450 image visualization with `ants.plot(...)`. This function enables multi-slice and multi-
451 orientation rendering with optional overlays and label maps.

452 4.2 Mapping fMOST data to AllenCCFv3

453 **Preprocessing.** Mapping fMOST data into the AllenCCFv3 presents unique challenges due
454 to its native ultra-high resolution and imaging artifacts common to the fMOST modality.
455 Each fMOST image can exceed a terabyte in size, with spatial resolutions far exceeding
456 those of the AllenCCFv3 ($25\text{ }\mu\text{m}$ isotropic). To reduce computational burden and prevent
457 resolution mismatch, each fMOST image is downsampled using cubic B-spline interpolation
458 via `ants.resample_image(...)` to match the template resolution.

459 Stripe artifacts (i.e., periodic intensity distortions caused by nonuniform sectioning or il-
460 lumination) are common in fMOST and can mislead deformable registration algorithms.
461 These were removed using a custom 3D notch filter (`remove_stripe_artifact(...)`) im-
462 plemented in the `CCFAlignmentToolkit` using SciPy frequency domain filtering. The filter
463 targets dominant stripe frequencies along a user-specified axis in the Fourier domain. In
464 addition, intensity inhomogeneity across sections, often arising from variable staining or
465 illumination, was corrected using N4 bias field correction.

466 **Template-based spatial normalization.** To facilitate reproducible mapping, we first
467 constructed a contralaterally symmetric average template from 30 fMOST brains and their
468 mirrored counterparts using ANTsX template-building tools. Because the AllenCCFv3 and
469 fMOST data differ substantially in both intensity contrast and morphology, direct deformable
470 registration between individual fMOST brains and the AllenCCFv3 was insufficiently robust.

471 Instead, we performed a one-time expert-guided label-driven registration between the aver-
472 age fMOST template and AllenCCFv3. This involved sequential alignment of seven manually
473 selected anatomical regions: 1) brain mask/ventricles, 2) caudate/putamen, 3) fimbria, 4)
474 posterior choroid plexus, 5) optic chiasm, 6) anterior choroid plexus, and 7) habenular com-
475 missure which were prioritized to enable coarse-to-fine correction of shape differences. Once
476 established, this fMOST-template-to-AllenCCFv3 transform was reused for all subsequent
477 specimens. Each new fMOST brain was then registered to the average fMOST template
478 using intensity-based registration, followed by concatenation of transforms to produce the
479 final mapping into AllenCCFv3 space.

480 **Mapping neuron projections.** A key advantage of fMOST imaging is its ability to support
481 single neuron projection reconstruction across the entire brain⁷⁸. Because these reconstruc-
482 tions are stored as 3D point sets aligned to the original fMOST volume, we applied the same
483 composite transform used for image alignment to the point data using ANTsX functional-
484 ity. This enables seamless integration of cellular morphology data into AllenCCFv3 space,
485 facilitating comparative analyses across specimens.

486 4.3 Mapping MERFISH data to AllenCCFv3

487 **Preprocessing.** MERFISH data are acquired as a series of 2D tissue sections, each com-
488 prising spatially localized gene expression measurements at subcellular resolution. To enable
489 3D mapping to the AllenCCFv3, we first constructed anatomical reference images by aggre-
490 gating the number of detected transcripts per voxel across all probes within each section.
491 These 2D projections were resampled to a resolution of $10 \mu m \times 10 \mu m$ to match the in-plane
492 resolution of the AllenCCFv3.

493 Sections were coarsely aligned using manually annotated dorsal and ventral midline points,
494 allowing initial volumetric reconstruction. However, anatomical fidelity remained limited by
495 variation in section orientation, spacing, and tissue loss. To further constrain alignment and
496 enable deformable registration, we derived region-level anatomical labels directly from the
497 gene expression data.

498 **Label creation.** To assign region labels to the MERFISH data, we use a cell type cluster-
499 ing approach previously detailed⁴⁶. In short, manually dissected scRNAseq data was used
500 to establish the distribution of cell types present in each of the following major regions:
501 cerebellum, CTXsp, hindbrain, HPF, hypothalamus, isocortex, LSX, midbrain, OLF, PAL,
502 sAMY, STRd, STRv, thalamus and hindbrain. Clusters in the scRNA-seq dataset were then
503 used to assign similar clusters of cell types in the MERFISH data to the regions they are
504 predominantly found in the scRNA-seq data. To account for clusters that were found at
505 low frequency in regions outside its main region we calculated for each cell its 50 nearest
506 neighbors in physical space and reassigned each cell to the region annotation dominating its
507 neighborhood.

508 **Section matching via global alignment.** A major challenge was compensating for oblique
509 cutting angles and non-uniform section thickness, which distort the anatomical shape and
510 spacing of the reconstructed volume. Rather than directly warping the MERFISH data
511 into atlas space, we globally aligned the AllenCCFv3 to the MERFISH coordinate system.
512 This was done via an affine transformation followed by resampling of AllenCCFv3 sections
513 to match the number and orientation of MERFISH sections. This approach minimizes
514 interpolation artifacts in the MERFISH data and facilitates one-to-one section matching.

515 **Landmark-driven deformable alignment.** We used a 2.5D approach for fine alignment
516 of individual sections. In each MERFISH slice, deformable registration was driven by sequen-
517 tial alignment of anatomical landmarks between the label maps derived from MERFISH and
518 AllenCCFv3. A total of nine regions, including isocortical layers 2/3, 5, and 6, the striatum,
519 hippocampus, thalamus, and medial/lateral habenula, were registered in an empirically de-
520 termined order. After each round, anatomical alignment was visually assessed by an expert,
521 and the next structure was selected to maximize improvement in the remaining misaligned
522 regions.

523 The final transform for each section combined the global affine alignment and the per-
524 structure deformable registrations. These were concatenated to generate a 3D mapping from
525 the original MERFISH space to the AllenCCFv3 coordinate system. Once established, the
526 composite mapping enables direct transfer of gene-level and cell-type data from MERFISH

527 into atlas space, allowing integration with other imaging and annotation datasets.

528 4.4 DevCCF velocity flow transformation model

529 The Developmental Common Coordinate Framework (DevCCF)¹⁶ provides a discrete set of
530 age-specific templates that temporally sample the developmental trajectory. To model this
531 biological progression more continuously, we introduce a velocity flow-based paradigm for in-
532 ferring diffeomorphic transformations between developmental stages. This enables anatomi-
533 cally plausible estimation of intermediate templates or mappings at arbitrary timepoints
534 between the E11.5 and P56 endpoints of the DevCCF. Our approach builds on established
535 insights from time-varying diffeomorphic registration⁶⁶, where a velocity field governs the
536 smooth deformation of anatomical structures over time. Importantly, the framework is ex-
537 tensible and can naturally accommodate additional timepoints for the potential expansion
538 of the DevCCF.

539 **Point sampling and region correspondence.** We first coalesced the anatomical labels
540 across the seven DevCCF templates (E11.5, E13.5, E15.5, E18.5, P4, P14, P56) into 26
541 common structures that could be consistently identified across development. These include
542 major brain regions such as the cortex, cerebellum, hippocampus, midbrain, and ventricles.
543 For each successive pair of templates, we performed multi-label deformable registration us-
544 ing ANTsX to generate forward and inverse transforms between anatomical label volumes.
545 From the P56 space, we randomly sampled approximately 1e6 points within and along the
546 boundaries of each labeled region and propagated them through each pairwise mapping step
547 (e.g., P56 → P14, P14 → P4, . . . , E13.5 → E11.5). This procedure created time-indexed
548 point sets tracing the spatial evolution of each region.

549 **Velocity field fitting.** Using these point sets, we fit a continuous velocity field over develop-
550 mental time using a generalized B-spline scattered data approximation method⁸⁷. The field
551 was parameterized over a log-scaled time axis to ensure finer temporal resolution during early
552 embryonic stages, where morphological changes are most rapid. Optimization proceeded for
553 approximately 125 iterations, minimizing the average Euclidean norm between transformed
554 points at each step. Ten integration points were used to ensure numerical stability. The

555 result is a smooth, differentiable vector field that defines a diffeomorphic transform between
556 any two timepoints within the template range.

557 **Applications and availability.** This velocity model can be used to estimate spa-
558 tial transformations between any pair of developmental stages—even those for which
559 no empirical template exists—allowing researchers to create interpolated atlases, align
560 new datasets, or measure continuous structural changes. It also enables developmental
561 alignment of multi-modal data (e.g., MRI to LSFM) by acting as a unifying spatiotem-
562 poral scaffold. The underlying components for velocity field fitting and integration
563 are implemented in ITK, and the complete workflow is accessible in both ANTsPy
564 (`ants.fit_time_varying_transform_to_point_sets(...)`) and ANTsR. In addition
565 the availability of the DevCCF use case, self-contained examples and usage tutorials are
566 provided in our public codebase.

567 4.5 Automated brain extraction and parcellation with ANTsXNet

568 To support template-based deep learning approaches for structural brain extraction and par-
569 cellation, we implemented dedicated pipelines using the ANTsXNet framework. ANTsXNet
570 comprises open-source deep learning libraries in both Python (ANTsPyNet) and R (ANTsR-
571 Net) that interface with the broader ANTsX ecosystem and are built on TensorFlow/Keras.
572 Our mouse brain pipelines mirror existing ANTsXNet tools for human imaging but are
573 adapted for species-specific anatomical variation, lower SNR, and heterogeneous acquisition
574 protocols.

575 4.5.1 Deep learning training setup

576 All network-based approaches were implemented using a standard U-net⁸⁸ architecture and
577 hyperparameters previously evaluated in ANTsXNet pipelines for human brain imaging⁴⁵.
578 This design follows the ‘no-new-net’ principle⁸⁹, which demonstrates that a well-configured,
579 conventional U-net can achieve robust and competitive performance across a wide range of
580 biomedical segmentation tasks with little to no architectural modifications from the original.

581 Both networks use a 3D U-net architecture implemented in TensorFlow/Keras, with five
582 encoding/decoding levels and skip connections. The loss function combined Dice and cate-
583 gorical cross-entropy terms. Training used a batch size of 4, Adam optimizer with an initial
584 learning rate of 2e-4, and early stopping based on validation loss. Training was performed on
585 an NVIDIA DGX system ($4 \times$ Tesla V100 GPUs, 256 GB RAM). Model weights and prepro-
586 cessing routines are shared across ANTsPyNet and ANTsRNet to ensure reproducibility and
587 language portability. For both published and unpublished trained networks available through
588 ANTsXNet, all training scripts and data augmentation generators are publicly available at
589 <https://github.com/ntustison/ANTsXNetTraining>.

590 **Data augmentation.** Robust data augmentation was critical to generalization across scan-
591 ners, contrast types, and resolutions. We applied both intensity- and shape-based augmen-
592 tation strategies:

593 • *Intensity augmentations:*

- 594 – Gaussian, Poisson, and salt-and-pepper noise:
595 `ants.add_noise_to_image(...)`
596 – Simulated intensity inhomogeneity via bias field modeling⁵¹:
597 `antspynet.simulate_bias_field(...)`
598 – Histogram warping to simulate contrast variation⁹⁰:
599 `antspynet.histogram_warp_image_intensities(...)`

600 • *Shape augmentations:*

- 601 – Random nonlinear deformations and affine transforms:
602 `antspynet.randomly_transform_image_data(...)`
603 – Anisotropic resampling across axial, sagittal, and coronal planes:
604 `ants.resample_image(...)`

605 **4.5.2 Brain extraction**

606 We originally trained a mouse-specific brain extraction model on two manually masked
607 T2-weighted templates, generated from public datasets^{68,69}. One of the templates was
608 constructed from orthogonal 2D acquisitions using B-spline-based volumetric synthesis via
609 `ants.fit_bspline_object_to_scattered_data(...)`. Normalized gradient magnitude
610 was used as a weighting function to emphasize boundaries during reconstruction⁸⁷.

611 This training strategy provides strong spatial priors despite limited data by leveraging high-
612 quality template images and aggressive augmentation to mimic population variability. Dur-
613 ing the development of this work, the network was further refined through community en-
614 gagement. A user from a U.S.-based research institute applied this publicly available (but
615 then unpublished) brain extraction tool to their own mouse MRI dataset. Based on feedback
616 and iterative collaboration with the ANTsX team, the model was retrained and improved to
617 better generalize to additional imaging contexts. This reflects our broader commitment to
618 community-driven development and responsiveness to user needs across diverse mouse brain
619 imaging scenarios.

620 The final trained network is available via ANTsXNet through the function
621 `antspynet.mouse_extraction(...)`. Additionally, both template/mask pairs are
622 accessible via ANTsXNet. For example, one such image pair is available via:

- 623 • Template:

624 `antspynet.get_antsxnet_data("bsplineT2MouseTemplate")`

- 625 • Brain mask:

626 `antspynet.get_antsxnet_data("bsplineT2MouseTemplateBrainMask")`

627 **4.5.3 Brain parcellation**

628 For brain parcellation, we trained a 3D U-net model using the DevCCF P56 T2-weighted
629 template and anatomical segmentations derived from AllenCCFv3. This template-based
630 training strategy enables the model to produce accurate, multi-region parcellations without
631 requiring large-scale annotated subject data.

632 To normalize intensity across specimens, input images were preprocessed using rank-based
633 intensity normalization (`ants.rank_intensity(...)`). Spatial harmonization was achieved
634 through affine and deformable alignment of each extracted brain to the P56 template prior
635 to inference. In addition to the normalized image input, the network also receives prior
636 probability maps derived from the atlas segmentations, providing additional spatial context.
637 This general parcellation deep learning framework has also been applied in collaboration
638 with other groups pursuing related but distinct projects. In one case, a model variant was
639 adapted for T2-weighted MRI using an alternative anatomical labeling scheme; in another,
640 a separate model was developed for serial two-photon tomography (STPT) with a different
641 parcellation set. All three models are accessible through a shared interface in ANTsXNet:
642 `antspynet.mouse_brain_parcellation(...)`. Ongoing work is further extending this ap-
643 proach to embryonic mouse brain data. These independent efforts reflect broader community
644 interest in adaptable parcellation tools and reinforce the utility of ANTsXNet as a platform
645 for reproducible, extensible deep learning workflows.

646 4.5.4 Evaluation and reuse

647 To assess model generalizability, both the brain extraction and parcellation networks were
648 evaluated on an independent longitudinal dataset comprising multiple imaging sessions with
649 varied acquisition parameters⁷⁰. Although each label or imaging modality required re-
650 training, the process was streamlined by the reusable ANTsX infrastructure enabled by
651 rapid adaptation with minimal overhead. These results illustrate the practical benefits of a
652 template-based, low-shot strategy and modular deep learning framework. All trained mod-
653 els, associated training scripts, and supporting resources are openly available and designed
654 for straightforward integration into ANTsX workflows.

655 **Data Availability**

656 The following datasets were used in this study and are publicly available:

- 657 • **Allen Common Coordinate Framework (AllenCCFv3):** Available from the Allen
658 Institute for Brain Science at <https://atlas.brain-map.org/atlas>.
- 659 • **Developmental Common Coordinate Framework (DevCCF) MRI and LSFM**
660 datasets: Publicly available via the Kim Lab <https://kimlab.io/home/projects/>
661 [DevCCF/index.html](#).
- 662 • **MERFISH spatial transcriptomics data:** Previously published⁴⁶ [https://portal.](https://portal.brain-map.org)
663 [brain-map.org](#).
- 664 • **Developmental datasets for brain extraction and segmentation:**
 - 665 – High-resolution MRI data of brain C57BL/6 and BTBR mice in three different
666 anatomical views: <https://data.mendeley.com/datasets/dz9x23fttt/1>.
 - 667 – CAMRI Mouse Brain Data: [https://openneuro.org/datasets/ds002868/versions/](https://openneuro.org/datasets/ds002868/versions/1.0.1)
668 [1.0.1](#)
- 669 • **Evaluation dataset for brain extraction and segmentation:** A longitudinal
670 microstructural MRI dataset in healthy C57Bl/6 mice at 9.4 Tesla <https://www.fdr-dfdr.ca/repo/dataset/9ea832ad-7f36-4e37-b7ac-47167c0001c1>.
- 672 • **ANTsXNet-pretrained templates and models:** Available through ANTsPy at
673 <https://github.com/ANTsX/ANTsPyNet>.

674 **Code Availability**

675 All processing pipelines and supporting code are openly available at:

- 676 • <https://github.com/ntustison/ANTsXMouseBrainMapping> (DevCCF velocity model
677 and deep learning parcellation). Also contains the text, scripts, and data to reproduce
678 the manuscript (including figures).
- 679 • <https://github.com/dontminchenit/CCFAlignmentToolkit> (MERFISH and fMOST
680 workflows)

⁶⁸¹ **Inclusion and Ethics Statement**

⁶⁸² All imaging data were obtained from publicly available sources that were collected in ac-
⁶⁸³ cordance with institutional animal care and use committee protocols and relevant ethical
⁶⁸⁴ regulations. The authors affirm that all analyses were conducted using open, reproducible
⁶⁸⁵ methods and that no exclusionary criteria were applied based on sex, age, or genetic back-
⁶⁸⁶ ground.

687 **Acknowledgments**

688 Support for the research reported in this work includes funding from the National Institute
689 of Biomedical Imaging and Bioengineering (R01-EB031722) and National Institute of Mental
690 Health (RF1-MH124605, U24-MH114827, and NIH RF1MH124605 to Y.K.).

691 We also acknowledge the data contribution of Dr. Adam Raikes (GitHub @araikes) of the
692 Center for Innovation in Brain Science at the University of Arizona for refining the weights
693 of the mouse brain extraction network.

⁶⁹⁴ **Author contributions**

⁶⁹⁵ N.T., M.C., and J.G. wrote the main manuscript text and figures. M.C., M.K., R.D., S.S.,
⁶⁹⁶ Q.W., L.G., J.D., C.G., and J.G. developed the Allen registration pipelines. N.T., F.K.,
⁶⁹⁷ J.G., and Y.K. developed the time-varying velocity transformation model for the DevCCF.
⁶⁹⁸ N.T. and M.T. developed the brain parcellation and cortical thickness methodology. All
⁶⁹⁹ authors reviewed the manuscript.

700 **References**

- 701 1. Keller, P. J. & Ahrens, M. B. Visualizing whole-brain activity and development at
the single-cell level using light-sheet microscopy. *Neuron* **85**, 462–83 (2015).
- 702 2. La Manno, G. *et al.* Molecular architecture of the developing mouse brain. *Nature*
596, 92–96 (2021).
- 703 3. Wen, L. *et al.* Single-cell technologies: From research to application. *Innovation
(Camb)* **3**, 100342 (2022).
- 704 4. Oh, S. W. *et al.* A mesoscale connectome of the mouse brain. *Nature* **508**, 207–14
(2014).
- 705 5. Gong, H. *et al.* Continuously tracing brain-wide long-distance axonal projections in
mice at a one-micron voxel resolution. *Neuroimage* **74**, 87–98 (2013).
- 706 6. Li, A. *et al.* Micro-optical sectioning tomography to obtain a high-resolution atlas of
the mouse brain. *Science* **330**, 1404–8 (2010).
- 707 7. Ueda, H. R. *et al.* Tissue clearing and its applications in neuroscience. *Nat Rev
Neurosci* **21**, 61–79 (2020).
- 708 8. Ståhl, P. L. *et al.* Visualization and analysis of gene expression in tissue sections by
spatial transcriptomics. *Science* **353**, 78–82 (2016).
- 709 9. Burgess, D. J. Spatial transcriptomics coming of age. *Nat Rev Genet* **20**, 317 (2019).
- 710 10. Hardwick, S. A. *et al.* Single-nuclei isoform RNA sequencing unlocks barcoded exon
connectivity in frozen brain tissue. *Nature biotechnology* **40**, 1082–1092 (2022).
- 711 11. Hawrylycz, M. *et al.* A guide to the BRAIN initiative cell census network data
ecosystem. *PLoS biology* **21**, e3002133 (2023).
- 712 12. Wang, Q. *et al.* The allen mouse brain common coordinate framework: A 3D reference
atlas. *Cell* **181**, 936–953.e20 (2020).
- 713 13. Perens, J. *et al.* An optimized mouse brain atlas for automated mapping and quantification
of neuronal activity using iDISCO+ and light sheet fluorescence microscopy.
Neuroinformatics **19**, 433–446 (2021).
- 714 14. Ma, Y. *et al.* A three-dimensional digital atlas database of the adult C57BL/6J mouse
brain by magnetic resonance microscopy. *Neuroscience* **135**, 1203–1215 (2005).

- 715 15. Qu, L. *et al.* Cross-modal coherent registration of whole mouse brains. *Nature Methods* **19**, 111–118 (2022).
- 716 16. Kronman, F. N. *et al.* [Developmental mouse brain common coordinate framework](#). *Nat Commun* **15**, 9072 (2024).
- 717 17. Chuang, N. *et al.* An MRI-based atlas and database of the developing mouse brain. *Neuroimage* **54**, 80–89 (2011).
- 718 18. Dries, R. *et al.* Advances in spatial transcriptomic data analysis. *Genome research* **31**, 1706–1718 (2021).
- 719 19. Ricci, P. *et al.* Removing striping artifacts in light-sheet fluorescence microscopy: A review. *Progress in biophysics and molecular biology* **168**, 52–65 (2022).
- 720 20. Agarwal, N., Xu, X. & Gopi, M. Robust registration of mouse brain slices with severe histological artifacts. in *Proceedings of the tenth indian conference on computer vision, graphics and image processing* 1–8 (2016).
- 721 21. Agarwal, N., Xu, X. & Gopi, M. Automatic detection of histological artifacts in mouse brain slice images. in *Medical computer vision and bayesian and graphical models for biomedical imaging: MICCAI 2016 international workshops, MCV and BAMBI, athens, greece, october 21, 2016, revised selected papers* 8 105–115 (Springer, 2017).
- 722 22. Tward, D. *et al.* 3d mapping of serial histology sections with anomalies using a novel robust deformable registration algorithm. in *International workshop on multimodal brain image analysis* 162–173 (Springer, 2019).
- 723 23. Cahill, L. S. *et al.* Preparation of fixed mouse brains for MRI. *Neuroimage* **60**, 933–939 (2012).
- 724 24. Biancalani, T. *et al.* [Deep learning and alignment of spatially resolved single-cell transcriptomes with tangram](#). *Nat Methods* **18**, 1352–1362 (2021).
- 725 25. Sunkin, S. M. *et al.* Allen brain atlas: An integrated spatio-temporal portal for exploring the central nervous system. *Nucleic acids research* **41**, D996–D1008 (2012).
- 726 26. Kim, Y. *et al.* Brain-wide maps reveal stereotyped cell-type-based cortical architecture and subcortical sexual dimorphism. *Cell* **171**, 456–469 (2017).

- 727 27. Fürth, D. *et al.* An interactive framework for whole-brain maps at cellular resolution. *Nat Neurosci* **21**, 139–149 (2018).
- 728 28. Li, Y. *et al.* mBrainAligner-web: A web server for cross-modal coherent registration of whole mouse brains. *Bioinformatics* **38**, 4654–4655 (2022).
- 729 29. Puchades, M. A., Csucs, G., Ledergerber, D., Leergaard, T. B. & Bjaalie, J. G. Spatial registration of serial microscopic brain images to three-dimensional reference atlases with the QuickNII tool. *PloS one* **14**, e0216796 (2019).
- 730 30. Eastwood, B. S. *et al.* Whole mouse brain reconstruction and registration to a reference atlas with standard histochemical processing of coronal sections. *Journal of Comparative Neurology* **527**, 2170–2178 (2019).
- 731 31. Ni, H. *et al.* A robust image registration interface for large volume brain atlas. *Sci Rep* **10**, 2139 (2020).
- 732 32. Pallast, N. *et al.* Processing pipeline for atlas-based imaging data analysis of structural and functional mouse brain MRI (AIDAmri). *Front Neuroinform* **13**, 42 (2019).
- 733 33. Celestine, M., Nadkarni, N. A., Garin, C. M., Bougacha, S. & Dhenain, M. Sammba-MRI: A library for processing SmAll-MaMmal BrAin MRI data in python. *Front Neuroinform* **14**, 24 (2020).
- 734 34. Ioanas, H.-I., Marks, M., Zerbi, V., Yanik, M. F. & Rudin, M. An optimized registration workflow and standard geometric space for small animal brain imaging. *Neuroimage* **241**, 118386 (2021).
- 735 35. Aggarwal, M., Zhang, J., Miller, M. I., Sidman, R. L. & Mori, S. Magnetic resonance imaging and micro-computed tomography combined atlas of developing and adult mouse brains for stereotaxic surgery. *Neuroscience* **162**, 1339–1350 (2009).
- 736 36. Chandrashekhar, V. *et al.* CloudReg: Automatic terabyte-scale cross-modal brain volume registration. *Nature methods* **18**, 845–846 (2021).
- 737 37. Jin, M. *et al.* SMART: An open-source extension of WholeBrain for intact mouse brain registration and segmentation. *eNeuro* **9**, (2022).
- 738 38. Negwer, M. *et al.* FriendlyClearMap: An optimized toolkit for mouse brain mapping and analysis. *Gigascience* **12**, (2022).

- 739 39. Lin, W. *et al.* Whole-brain mapping of histaminergic projections in mouse brain. *Proceedings of the National Academy of Sciences* **120**, e2216231120 (2023).
- 740 40. Zhang, M. *et al.* Spatially resolved cell atlas of the mouse primary motor cortex by MERFISH. *Nature* **598**, 137–143 (2021).
- 741 41. Shi, H. *et al.* Spatial atlas of the mouse central nervous system at molecular resolution. *Nature* **622**, 552–561 (2023).
- 742 42. Zhang, Y. *et al.* Reference-based cell type matching of *in situ* image-based spatial transcriptomics data on primary visual cortex of mouse brain. *Scientific Reports* **13**, 9567 (2023).
- 743 43. Klein, S., Staring, M., Murphy, K., Viergever, M. A. & Pluim, J. P. W. [Elastix: A toolbox for intensity-based medical image registration](#). *IEEE Trans Med Imaging* **29**, 196–205 (2010).
- 744 44. Fedorov, A. *et al.* 3D slicer as an image computing platform for the quantitative imaging network. *Magnetic resonance imaging* **30**, 1323–1341 (2012).
- 745 45. Tustison, N. J. *et al.* [The ANTsX ecosystem for quantitative biological and medical imaging](#). *Sci Rep* **11**, 9068 (2021).
- 746 46. Yao, Z. *et al.* [A high-resolution transcriptomic and spatial atlas of cell types in the whole mouse brain](#). *Nature* **624**, 317–332 (2023).
- 747 47. Pagani, M., Damiano, M., Galbusera, A., Tsafaris, S. A. & Gozzi, A. Semi-automated registration-based anatomical labelling, voxel based morphometry and cortical thickness mapping of the mouse brain. *Journal of neuroscience methods* **267**, 62–73 (2016).
- 748 48. Anderson, R. J. *et al.* [Small animal multivariate brain analysis \(SAMBA\) - a high throughput pipeline with a validation framework](#). *Neuroinformatics* **17**, 451–472 (2019).
- 749 49. Allan Johnson, G. *et al.* Whole mouse brain connectomics. *Journal of Comparative Neurology* **527**, 2146–2157 (2019).
- 750 50. Avants, B. B., Epstein, C. L., Grossman, M. & Gee, J. C. [Symmetric diffeomorphic image registration with cross-correlation: Evaluating automated labeling of elderly and neurodegenerative brain](#). *Med Image Anal* **12**, 26–41 (2008).

- 751 51. Tustison, N. J. *et al.* N4ITK: Improved N3 bias correction. *IEEE Trans Med Imaging* **29**, 1310–20 (2010).
- 752 52. Bajcsy, R. & Broit, C. Matching of deformed images. in *Sixth International Conference on Pattern Recognition (ICPR'82)* 351–353 (1982).
- 753 53. Bajcsy, R. & Kovacic, S. Multiresolution elastic matching. *Computer Vision, Graphics, and Image Processing* **46**, 1–21 (1989).
- 754 54. Gee, J. C., Reivich, M. & Bajcsy, R. Elastically deforming 3D atlas to match anatomical brain images. *J Comput Assist Tomogr* **17**, 225–36 (1993).
- 755 55. Klein, A. *et al.* Evaluation of 14 nonlinear deformation algorithms applied to human brain MRI registration. *Neuroimage* **46**, 786–802 (2009).
- 756 56. Murphy, K. *et al.* Evaluation of registration methods on thoracic CT: The EMPIRE10 challenge. *IEEE Trans Med Imaging* **30**, 1901–20 (2011).
- 757 57. Baheti, B. *et al.* The brain tumor sequence registration challenge: Establishing correspondence between pre-operative and follow-up MRI scans of diffuse glioma patients. (2021).
- 758 58. Roston, R. A., Tustison, N. J. & Maga, A. M. Anatomy-aware, label-informed approach improves image registration for challenging datasets. *bioRxiv* (2025) doi:10.1101/2025.08.11.669599.
- 759 59. Avants, B. B. *et al.* The optimal template effect in hippocampus studies of diseased populations. *Neuroimage* **49**, 2457–66 (2010).
- 760 60. Avants, B. B., Tustison, N. J., Wu, J., Cook, P. A. & Gee, J. C. An open source multivariate framework for n-tissue segmentation with evaluation on public data. *Neuroinformatics* **9**, 381–400 (2011).
- 761 61. Manjón, J. V., Coupé, P., Martí-Bonmatí, L., Collins, D. L. & Robles, M. Adaptive non-local means denoising of MR images with spatially varying noise levels. *J Magn Reson Imaging* **31**, 192–203 (2010).
- 762 62. Wang, H. *et al.* Multi-atlas segmentation with joint label fusion. *IEEE Trans Pattern Anal Mach Intell* **35**, 611–23 (2013).

- 763 63. Tustison, N. J. *et al.* Optimal symmetric multimodal templates and concatenated random forests for supervised brain tumor segmentation (simplified) with *ANTsR*. *Neuroinformatics* (2014) doi:[10.1007/s12021-014-9245-2](https://doi.org/10.1007/s12021-014-9245-2).
- 764 64. Tustison, N. J., Yang, Y. & Salerno, M. **Advanced normalization tools for cardiac motion correction**. in *Statistical atlases and computational models of the heart - imaging and modelling challenges* (eds. Camara, O. et al.) vol. 8896 3–12 (Springer International Publishing, 2015).
- 765 65. McCormick, M., Liu, X., Jomier, J., Marion, C. & Ibanez, L. **ITK: Enabling reproducible research and open science**. *Front Neuroinform* **8**, 13 (2014).
- 766 66. Beg, M. F., Miller, M. I., Trouvé, A. & Younes, L. **Computing large deformation metric mappings via geodesic flows of diffeomorphisms**. *International Journal of Computer Vision* **61**, 139–157 (2005).
- 767 67. Tustison, N. J. & Avants, B. B. **Explicit B-spline regularization in diffeomorphic image registration**. *Front Neuroinform* **7**, 39 (2013).
- 768 68. Hsu, L.-M. *et al.* CAMRI mouse brain MRI data.
- 769 69. Reshetnikov, V. *et al.* High-resolution MRI data of brain C57BL/6 and BTBR mice in three different anatomical views.
- 770 70. Rahman, N., Xu, K., Budde, M. D., Brown, A. & Baron, C. A. **A longitudinal microstructural MRI dataset in healthy C57Bl/6 mice at 9.4 tesla**. *Sci Data* **10**, 94 (2023).
- 771 71. Liu, J. *et al.* **Concordance of MERFISH spatial transcriptomics with bulk and single-cell RNA sequencing**. *Life Sci Alliance* **6**, (2023).
- 772 72. Stringer, C., Wang, T., Michaelos, M. & Pachitariu, M. **Cellpose: A generalist algorithm for cellular segmentation**. *Nat Methods* **18**, 100–106 (2021).
- 773 73. Jia, H., Yap, P.-T., Wu, G., Wang, Q. & Shen, D. **Intermediate templates guided groupwise registration of diffusion tensor images**. *NeuroImage* **54**, 928–939 (2011).
- 774 74. Tang, S., Fan, Y., Wu, G., Kim, M. & Shen, D. **RABBIT: Rapid alignment of brains by building intermediate templates**. *NeuroImage* **47**, 1277–1287 (2009).

- 775 75. Dewey, B. E., Carass, A., Blitz, A. M. & Prince, J. L. Efficient multi-atlas registration using an intermediate template image. in *Proceedings of SPIE—the international society for optical engineering* vol. 10137 (NIH Public Access, 2017).
- 776 76. Perens, J. *et al.* Multimodal 3D mouse brain atlas framework with the skull-derived coordinate system. *Neuroinformatics* **21**, 269–286 (2023).
- 777 77. Rotolo, T., Smallwood, P. M., Williams, J. & Nathans, J. Genetically-directed, cell type-specific sparse labeling for the analysis of neuronal morphology. *PLoS One* **3**, e4099 (2008).
- 778 78. Peng, H. *et al.* Morphological diversity of single neurons in molecularly defined cell types. *Nature* **598**, 174–181 (2021).
- 779 79. Gong, H. *et al.* High-throughput dual-colour precision imaging for brain-wide connectome with cytoarchitectonic landmarks at the cellular level. *Nat Commun* **7**, 12142 (2016).
- 780 80. Wang, J. *et al.* Divergent projection patterns revealed by reconstruction of individual neurons in orbitofrontal cortex. *Neurosci Bull* **37**, 461–477 (2021).
- 781 81. Avants, B. B. *et al.* The Insight ToolKit image registration framework. *Front Neuroinform* **8**, 44 (2014).
- 782 82. Chon, U., Vanselow, D. J., Cheng, K. C. & Kim, Y. Enhanced and unified anatomical labeling for a common mouse brain atlas. *Nat Commun* **10**, 5067 (2019).
- 783 83. Tasic, B. *et al.* Adult mouse cortical cell taxonomy revealed by single cell transcriptomics. *Nat Neurosci* **19**, 335–46 (2016).
- 784 84. Bergmann, E., Gofman, X., Kavushansky, A. & Kahn, I. Individual variability in functional connectivity architecture of the mouse brain. *Commun Biol* **3**, 738 (2020).
- 785 85. Billot, B. *et al.* SynthSeg: Segmentation of brain MRI scans of any contrast and resolution without retraining. *Med Image Anal* **86**, 102789 (2023).
- 786 86. Rolfe, S. M., Whikehart, S. M. & Maga, A. M. Deep learning enabled multi-organ segmentation of mouse embryos. *Biol Open* **12**, bio059698 (2023).

- 787 87. Tustison, N. J. & Gee, J. C. Generalized n -d C^k B-spline scattered data approximation
with confidence values. in *Medical imaging and augmented reality* (eds. Yang, G.-Z.,
Jiang, T., Shen, D., Gu, L. & Yang, J.) 76–83 (Springer Berlin Heidelberg, 2006).
- 788 88. Falk, T. *et al.* U-net: Deep learning for cell counting, detection, and morphometry.
Nat Methods **16**, 67–70 (2019).
- 789 89. Isensee, F., Jaeger, P. F., Kohl, S. A. A., Petersen, J. & Maier-Hein, K. H. nnU-net:
A self-configuring method for deep learning-based biomedical image segmentation.
Nat Methods **18**, 203–211 (2021).
- 790 90. Tustison, N. J. *et al.* Image- versus histogram-based considerations in semantic seg-
mentation of pulmonary hyperpolarized gas images. *Magn Reson Med* **86**, 2822–2836
(2021).